INVESTIGATING THE SCATTERING MECHANISM IN LOW CALCIUM PYROXENE ZONES OVER THE BULLIALDUS CRATER ON MOON USING M[3] AND MINI-RF DATA

Akash[1a], Shashi Kumar[2b] and S. K. Srivastav[2c]

[1]Indian Institute of Technology (Indian School of Mines), Dhanbad, India

Email: akafore7@gmail.com

[2]Indian Institute of Remote sensing, Indian Space Research Organisation, Department of Space, Government of India, Dehradun, India

Email: {[b]shashi, [c]sksrivastav}@iirs.gov.in

Keywords: Moon Mineralogy Mapper, Mini-RF, Chandrayaan-1, Lunar Reconnaissance Orbiter, Low calcium pyroxenes, Scattering mechanism, Bullialdus crater

ABSTRACT

Remotely sensed spectroscopic and radar data have been studied by researchers for characterising the mineralogy and scattering properties of lunar surface to understand the geologic evolution of lunar crust. In this study, we investigate the scattering mechanism in the *low calcium pyroxene* (LCP) mineral bearing zones occurring on the lunar surface. Bullialdus crater, located in the south-western part of the moon, is taken as the test site. The data obtained from Moon Mineralogical Mapper (M[3]) on-board ISRO's Chandrayaan-1 lunar orbiter mission are used to find LCP zones using a spectral index, called as LCP index. The data from Miniature Radio Frequency (Mini-RF) instrument on-board NASA's Lunar Reconnaissance Orbiter (LRO) are used for characterising the scattering properties of the lunar surface using the Stokes parameters and different decomposition techniques *viz.,* m-δ, m-χ and H-α. The spectrally dominant LCP zones are mainly found in and around the central peak of the Bullialdus crater as also observed by earlier researchers with LCP index ranging from 0.01 to 0.13, majority within 0.08. Modified Gaussian Model (MGM) fit on the spectra indicates that 1 μm band is centred between 910-950 nm and 2 μm band is centred between 1830-1890 nm. Regression analysis indicates weak but statistically significant negative relation of LCP index with surface scattering, double bounce scattering, volume scattering and *circular polarisation ratio* (CPR); whereas, no relation is observed between LCP index and *entropy* (H) and mean α. Such study at different sites across the lunar surface is needed to gain better insights into understanding the scattering mechanism vis-a-vis lunar mineralogy.

1. INTRODUCTION

The Earth-based telescope observations, measurements from orbiting spacecrafts and lunar samples are the basis for the study of the element abundances in the moon (Carter et al., 2017; McLeod and Krekeler, 2017; Smith et al., 2017). Moon is a storage of different minerals and many rare elements (Day and Moynier, 2014; Moynier et al., 2010; Paniello et al., 2012; Wang and Jacobsen, 2016; Wiechert, 2001). Several unmanned missions to the Moon have helped the scientists all over the globe to find interesting results that helped studying the lunar surface and characterisation of lunar impact craters (Dhingra et al., 2017; Gault, 1970; Li et al., 2017). A number of impact craters are present on the surface of the moon like Bullialdus and Copernicus. When an impactor or heavenly body like meteorite strikes the solid surface of a planet with a very high velocity, a crater is formed. The materials then get sprayed in all directions on the Lunar surface (Krishna and Kumar, 2016; Osinski et al., 2011; Research Team and Kramer, 2014; Starr et al., 2017)

Different missions have been launched, including the India's maiden mission to moon (Chandrayaan-1), to explore the lunar surface and also to study the geographical features such as the craters (Pieters et al., 2009; Jin et al., 2013; Wang et al., 1995; Wang et al., 2017). Chandrayaan-1 was launched in October, 2008 and operated until August, 2009. The Moon Mineralogy Mapper (M[3]) was one of the payloads in the Chandrayaan-1 with the major objective of mineralogical mapping of the moon (Green et al., 2008; Pieters et al., 2009). NASA's Lunar Reconnaissance Orbiter (LRO), launched in June, 2009, carried a Miniature Radio-Frequency (MINI-RF) instrument (Vondrak et al., 2010; Robinson et al., 2010). The Mini-RF is a *synthetic aperture radar* (SAR) which is an example of hybrid polarimetric system designed to transmit circular polarization waves and receive linearly orthogonal polarization waves (Spudis et al., 2013; Nozette et al., 2010; Raney et al., 2011), and is useful to study scattering mechanism on the lunar surface.

The objective of this study is to explore the potential of Chandrayaan-1 M^3 data to map the *low calcium pyroxene* (LCP) zones and analyse the scattering mechanism of these zones using the LRO's Mini-RF data in the Bullialdus crater present on moon. Pyroxenes are mafic minerals consisting of silicon aluminium oxides with elements like calcium, magnesium or sodium substituting for silicon and aluminium. It is of two types, orthopyroxenes and clinopyroxenes (Adams, 1974; Wagner et al., 1987) and is the most common mineral in the solid bodies of the solar system. Orthopyroxenes are low calcium pyroxenes and clinopyroxenes have both low as well as high calcium content. Pyroxenes can be easily identified in near infrared region of the electromagnetic spectrum. The spectroscopic signature of pyroxenes consists of two strong absorption bands at 1 μm and 2 μm. The 2 μm absorption band has the absorption peak at 1900 nm in case of low calcium pyroxenes and 2300 nm in case of high calcium pyroxenes (Sunshine and Pieters, 1993). The main reason behind these strong absorption bands is the electronic transition happening because of the presence of Fe^{+2} in the octahedral cation sites of the pyroxenes (Sunshine et al., 1999).

2. STUDY AREA AND DATA USED

The study area selected for this study is the Bullialdus Crater, which is located in the south-western part of the moon having a diameter of 61 km and depth of 3.5 km. The central peak of Bullialdus is located in Mare Nubium at about 20.7ºS and 22.2ºW. It is an Eratosthenian aged crater. It consists of a higher outer rim and an inner wall and central peaks due to the impact.

Two types of data, Chandrayaan-1 M^3 data (Table-1) and LRO's Mini-RF data (Table 2), are downloaded from the Planetary Data System (PDS) Geoscience Node website (http://pds-geosciences.wustl.edu/).

Table 1: M^3 data description

Data Set	Date of Acquisition	Spatial resolution	Spectral resolution
M3G20090207T065039_V01_L2	07-02-2009	140 m/pixel	20-40 nm
M3G20090207T083836_V01_L2	07-02-2009	140 m/pixel	20-40 nm
M3G20090416T160201_V01_L2	16-04-2009	140 m/pixel	20-40 nm
M3G20090416T181121_V01_L2	16-04-2009	140 m/pixel	20-40 nm

Table2: Mini-RF data description

Product Name	Creation Date	Frequency	Resolution
LSZ 02644 2CD EKU 23S339 V1	27-05-2010	2.38 GHz (12.6 cm)	150 m
LSZ 02645 2CD EKU 20S338 V1	27-05-2010	2.38 GHz (12.6 cm)	150 m
LSZ 02646 2CD EKU 20S337 V1	27-05-2010	2.38 GHz (12.6 cm)	150 m
LSZ 02646 2CD EKU 16S339 V1	12-05-2010	2.38 GHz (12.6 cm)	150 m
LSZ 02646 2CD EKU 15S338 V1	27-01-2012	2.38 GHz (12.6 cm)	150 m
LSZ 02646 2CD EKU 15S337 V1	14-01-2011	2.38 GHz (12.6 cm)	150 m

3. METHODOLOGY

The methodology adopted to map the LCP bearing zones and analyse their scattering mechanism is shown in figure 1. The M^3 data around the Bullialdus crater are georeferenced using the datum file D_Moon_2000, GCS_Moon_2000, 0, 0, 0 and the ellipse file GCS_Moon_2000, 1737400.0, 1737400.0 (Barnes, 2016). After georeferencing, mosaicking is done and subset around the Bullialdus crater is taken (Fig. 2a). Similarly, subsetting and mosaicking are performed for the Mini-RF data (Fig. 2c). Continuum removal on spectra obtained from M^3 data is carried out followed by the calculation of parameters C1, C2, absorption wavelength and the continuum removed band depth (Klima et al., 2011; Horgan et al., 2014). Using these parameters, the LCP index is estimated over the central peak of Bullialdus crater(Klima et al., 2011). The compositional analysis is done over the same region using the Modified Gaussian Model (MGM) (Sunshine et al., 1999; NASA Reflectance Experiment Laboratory, 2016). Mini-RF data are used to calculate Stokes parameters from which Stokes child parameters are calculated (Kumar et al., 2016; Raney, 2016; Tomar et al., 2016). Stokes child parameters are then used to apply different decomposition techniques and the scattering mechanisms are retrieved. Finally, regression analysis is carried out to find out the relation between the LCP and different scattering components.

4. RESULT AND DICSUSSION

4.1 Low calcium pyroxene zones using M³ data

LCP index image obtained after applying the algorithm is shown in figure 2b. The bright patches in figure 2b are LCP zones.

The MGM (Sunshine and Pieters, 1993; Clénet et al., 2011) is applied on the M³ reflectance data which were collected from the pixel (20° 42' 3.78" S and 22° 11' 51.75" W) near to the central peak of the Bullialdus crater. The initial and final MGM firs are shown in figure 3. The initial and final absorption band parameters after applying the MGM to the spectral data are shown in table 3 and table 4, respectively. Based on the initial and final fits, it is found that 1 μm band is centred between 910 to 950 nm and the 2 μm band is centred between 1830 to 1890 nm, with relatively high Mg. The uncertainty for the 1 μm band is ±10 nm and for 2 μm band it is 20-50 nm which is somewhat large.
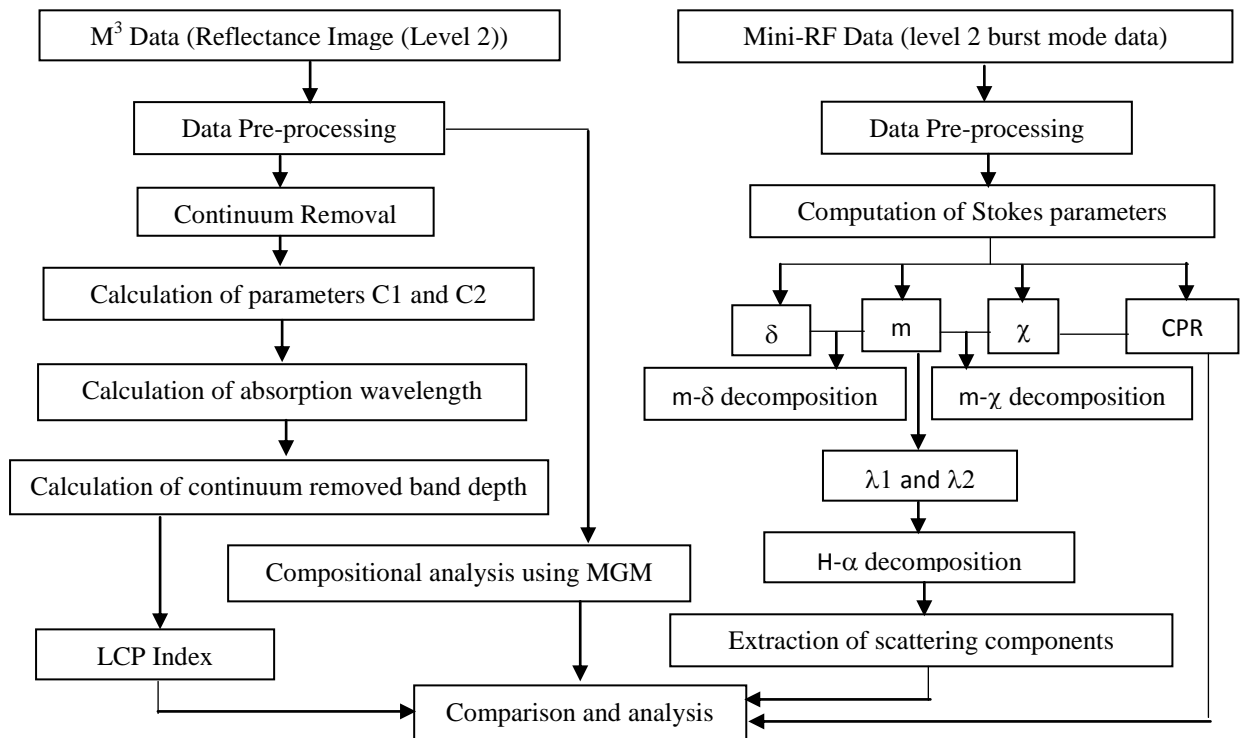
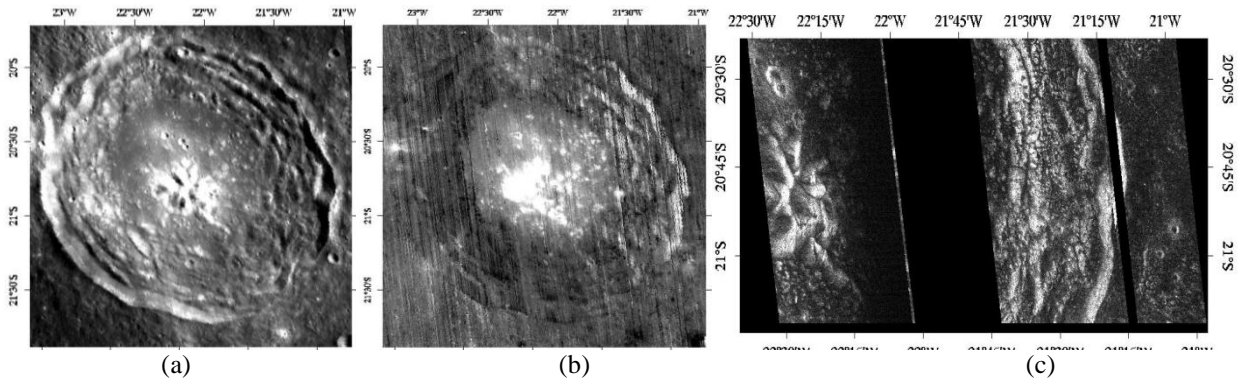

Figure 1: Flow diagram showing the methodology adopted

Figure 2: (a) Subset of M³ (band-6, 730.48 nm) data after mosaicking; (b) LCP image; and (c) mosaic of Mini-RF data (data portion is the data gap). The images obtained from both the sensors were converted into the same projection system i.e., sinusoidal projection with the pixel size as 70 m for proper comparison and analysis of the parameters.
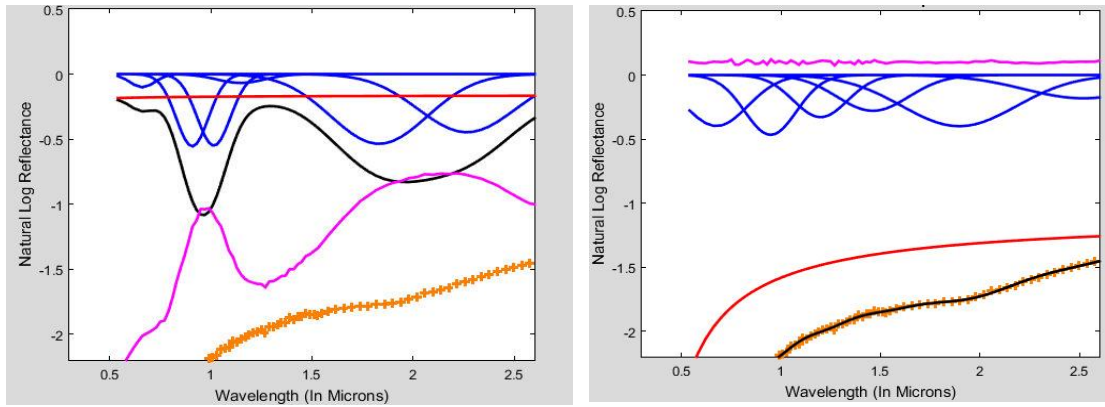
(a) Continuum (polynomial in wave number) offset: 0.85, slope: -1.0E-06, RMSE: 1.28

(b) Continuum (polynomial in wave number) offset: 0.33, slope: -1.28E-05, RMSE: 1.11E-02

Figure 3: (a) Initial MGM fit and (b) final MGM fit to the spectra of Bullialdus crater continuum. In the initial and final fits, the pink line indicates the residual error and the orange line indicates our spectra taken form Bullialdus crater, red line indicates the continuum, black line represents the fit and the blue line represents different absorption bands.

Table 3: Initial absorption parameters

Band Centre	FWHM	Band Strength
248.3219	94.8290	-1.0460
675.3828	371.8047	-0.3987
947.8606	307.0131	-0.4673
1198.7733	319.5314	-0.3290
1461.9813	424.9118	-0.2792
1896.0425	677.6958	-0.3999
2520.3581	699.9246	-0.1818

Table 4: Final absorption parameters

Band Centre	FWHM	Band Strength
248.3200	92.8490	-1.0460
661.5000	144.6300	-0.1020
908.4800	188.2600	-0.5560
1014.9800	192.9800	-0.5510
1147.6000	277.6800	-0.0680
1832.0000	560.4000	-0.5370
2266.1000	563.3500	-0.4480

4.2 Scattering information retrieval using Mini-RF data

Different Stokes child parameters are obtained (Fig. 4) and their range of values and mean are studied. The value of χ (shape of the polarization ellipse or ellipticity) ranges from -41.43 to 30.21 with the mean value of -0.15 (Fig. 4a). A lot of variation in the values is seen inside the crater. The Circular Polarization Ratio (CPR) ranges from 0.036 to 8.838 with the mean value of 0.81 (Fig. 4b). High values are observed over the central peak and comparatively lower values near the central peak. The value of δ (relative phase) ranges from -90.04 to 90.04 and the mean value is 6.83 (Fig. 4c). The *degree of polarization* (m) ranges from 0 to 0.94 and the mean value is 0.45 (Fig.4d). Lower values of m are found near the central peak of the crater. The value of mean α ranges from 20.07 to 72.25 and has the mean value of 45.52 (Fig. 4e). Comparatively lower values of mean α are found over the central peak of the crater. The value of H (Entropy) ranges from 0.17 to 0.99 and the mean value is 0.82 (Fig.4e). The higher values of H are found over the central peak and also near the central peak of the Bullialdus crater.

Different scattering components are retrieved using the Stokes parameters and are then compared with the LCP index. The value of surface scattering component of m-χ decomposition (SSMCHI) ranges from 0 to 0.90 and the mean value is 0.12 (Fig. 5a). The value of surface scattering component of m-δ decomposition (SSMDELTA), ranges from 0 to 0.95 with the mean value of 0.127 (Fig. 5b). The value of volume scattering component of m-χ decomposition (VSMCHI) ranges from 0.01 to 1.06 with the mean value of 0.18 (Fig. 5c). The value of volume scattering component of m-δ decomposition (VSMDELTA) ranges from 0.01 to 1.06 with the mean value of 0.18 (Fig. 5d). The value of double bounce scattering component of m-χ decomposition (DSMCHI) ranges from 0 to 0.82 and the mean value is 0.119 (Fig. 5e). The value of double bounce scattering component of m-δ decomposition (DSMDELTA) ranges from 0 to 0.80 and its mean value is 0.09 (Fig. 5f). In all the above cases, what we observe is that the value of the scattering components over the central peak is more than the values in the region near the central peak of the Bullialdus crater.
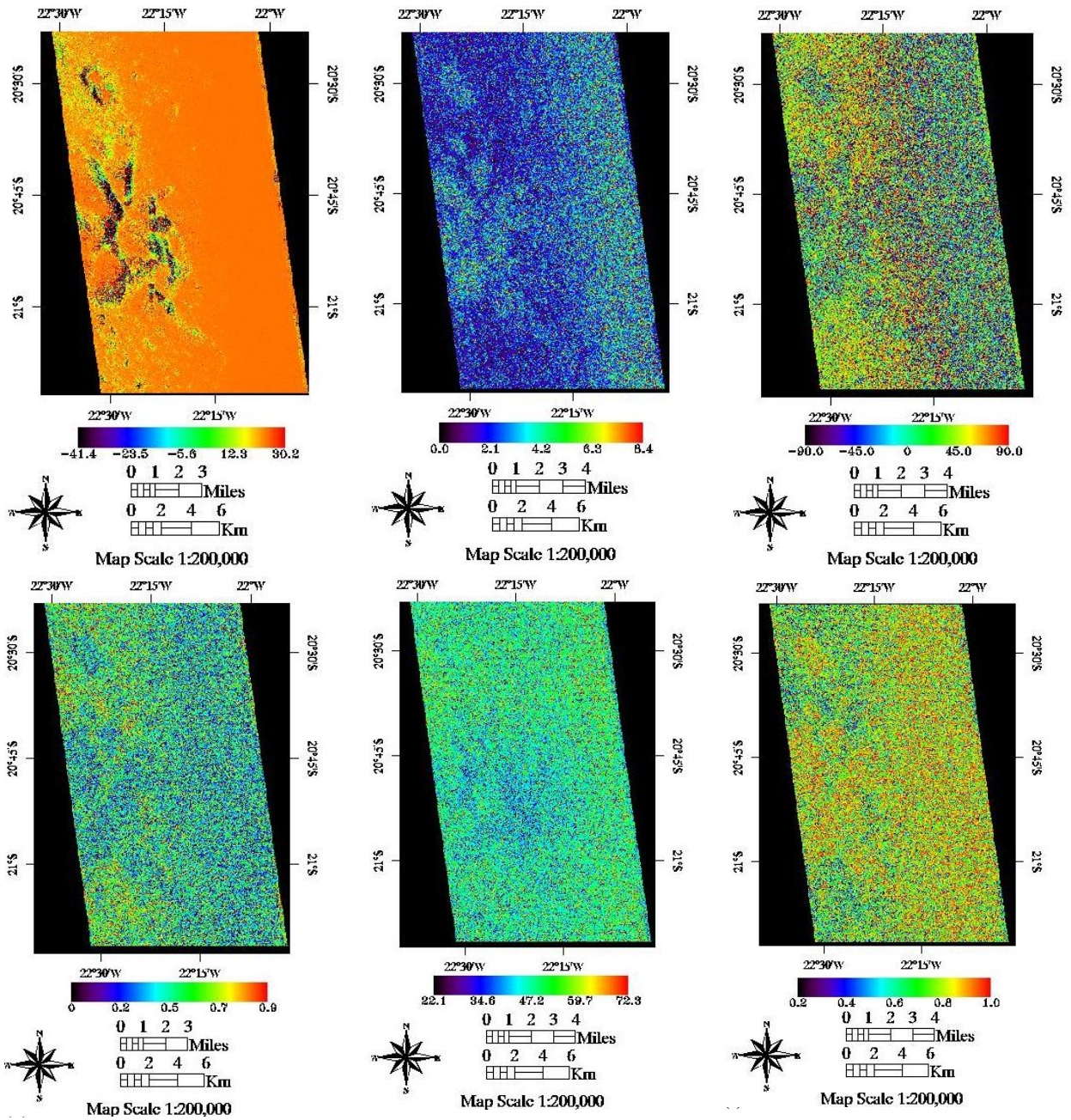
Figure 4: (a-d) Stokes child parameters, χ, CPR, δ and m; (e) mean α; and (f) H

4.3 Relation between LCP index and scattering components

To understand the relation between LCP index and scattering components and overall scattering mechanism, regression analysis is carried out between LCP index and scattering components obtained through different decomposition techniques; between LCP index and Stokes parameters; and between different scattering components (Fig. 6, Fig. 7). The analysis indicates that weak but statistically significant negative relation exists between LCP index with surface scattering, double bounce scattering, volume scattering and CPR. Strong positive relation is observed between surface and volume scattering. Entropy (H) and CPR have moderately strong positive relation. However, no relation is observed between LCP index and H and mean α.
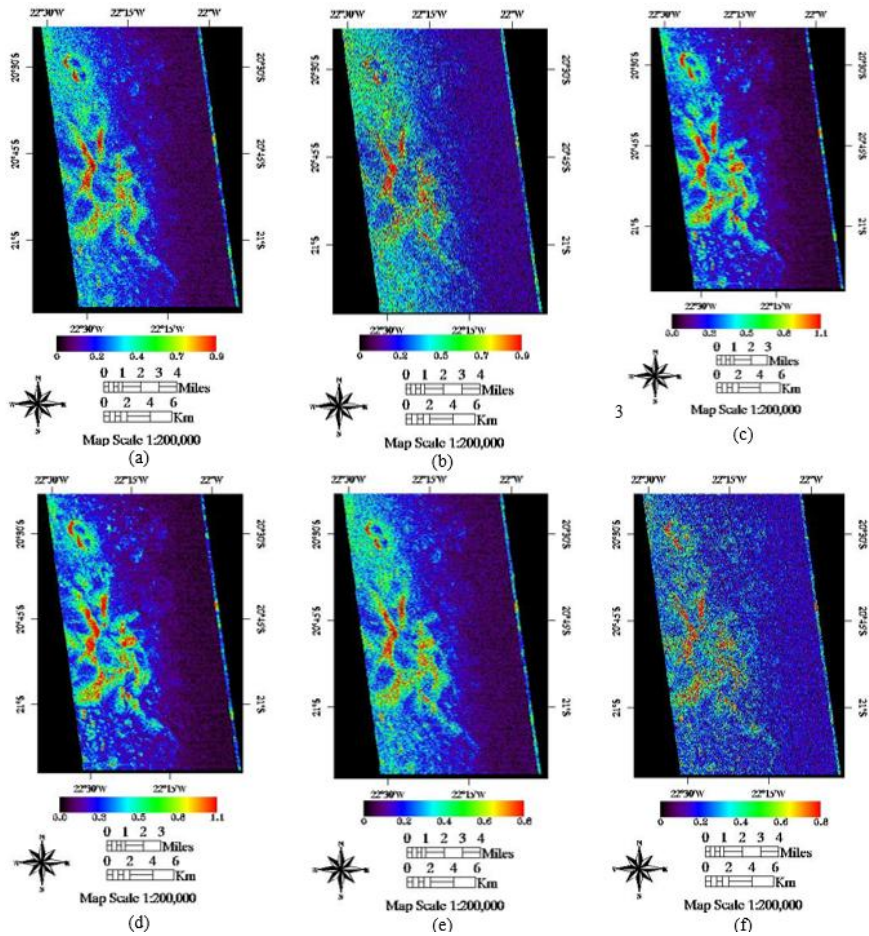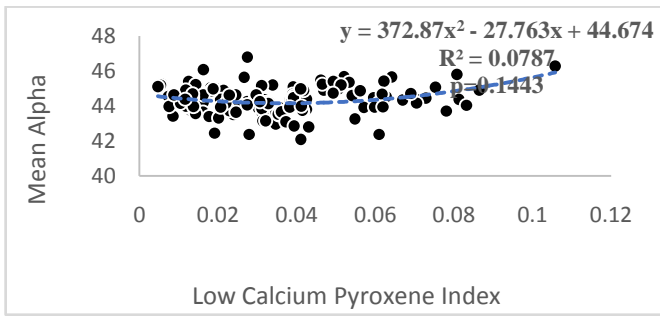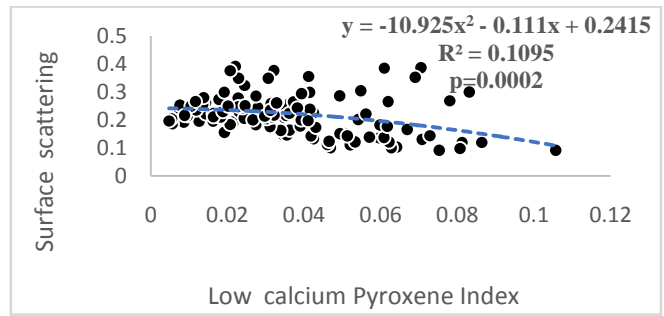
Figure 5: Surface scattering component retrieved from (a) m-χ decomposition and (b) m-δ decomposition; volume scattering component retrieved from (c) m-χ decomposition and (d) m-δ decomposition; and double bounce scattering retrieved from (e) m-χ decomposition and (f) m-δ decomposition
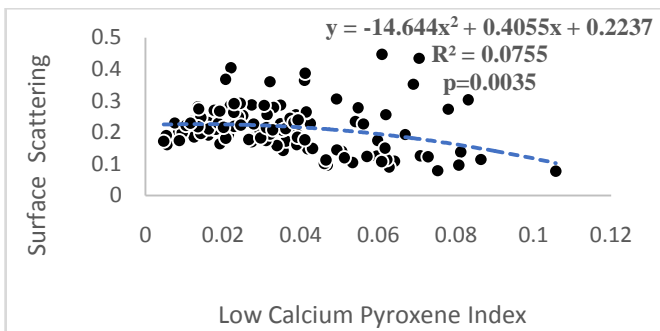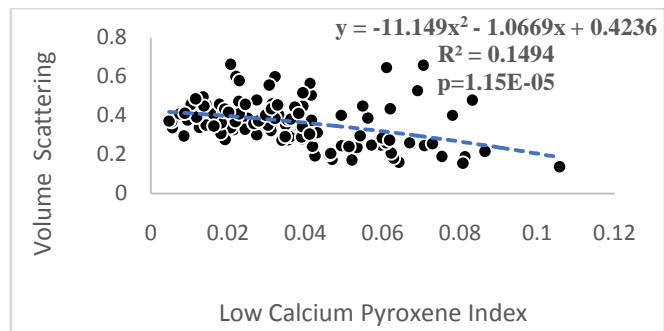

$y = -2.4242x + 0.9579$
$R^2 = 0.1091$
$p = 0.00035$

(a)

$y = -9.506x^2 - 0.2662x + 0.2345$
$R^2 = 0.1626$
$p = 4.97746E-06$

(b)

$y = -1.0261x + 0.2121$
$R^2 = 0.1284$
$p = 4.44451E-05$

(c)

$y = -0.1542x + 0.8559$
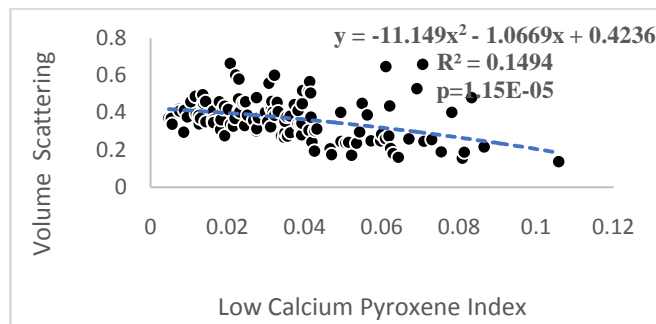$R^2 = 0.0146$
$p = 0.237$

(d)
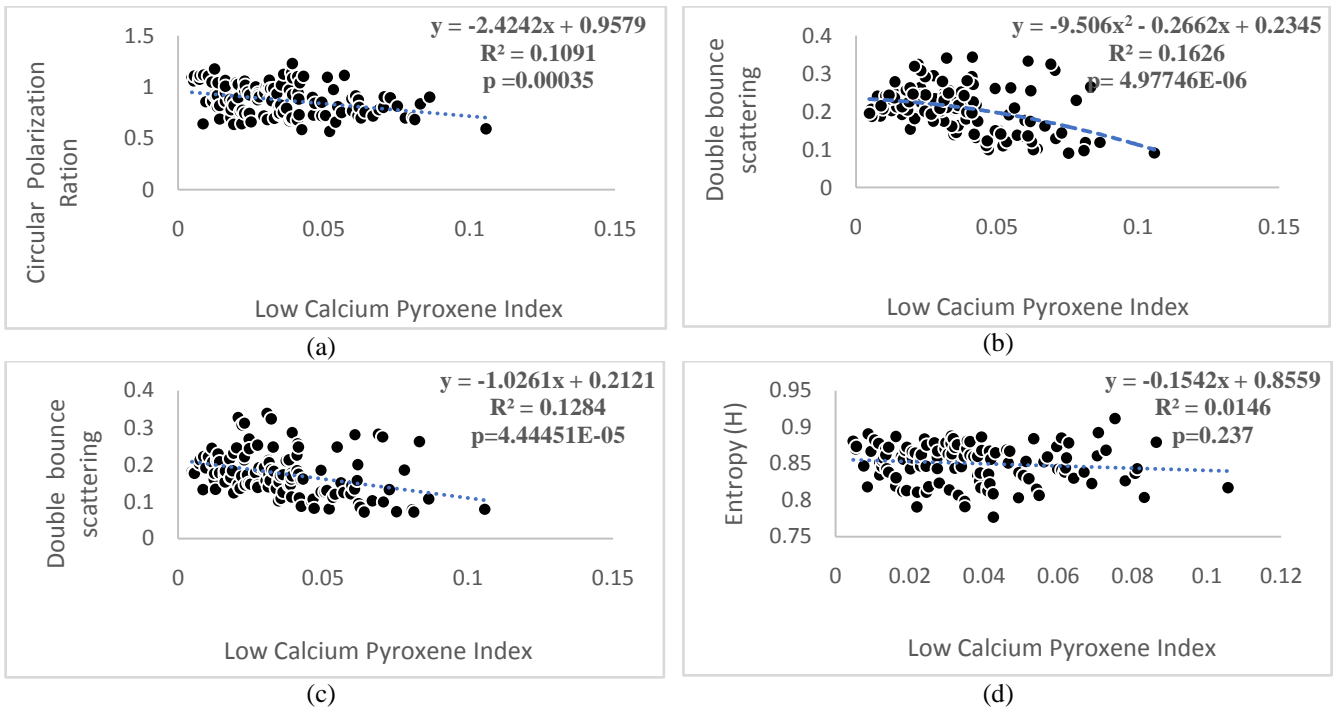
(e)

(f)

(g)


(h)


(i)

Figure 6: Plots between LCP and (a) CPR, (b) double bounce scattering of m-χ decomposition, (c) double bounce scattering of m-δ decomposition, (d) H, (e) mean α, (f) surface scattering component of m-χ decomposition, (g) surface scattering component m-δ decomposition, (h) volume scattering of m-χ decomposition, and (i) volume scattering through m-δ decomposition. Note: 95% confidence bound is considered for the calculation of "p"

(a)

(b)

$$y = -0.3246x^2 + 0.6677x + 0.5225$$
$$R^2 = 0.4069$$
$$p = 2.01E-11$$
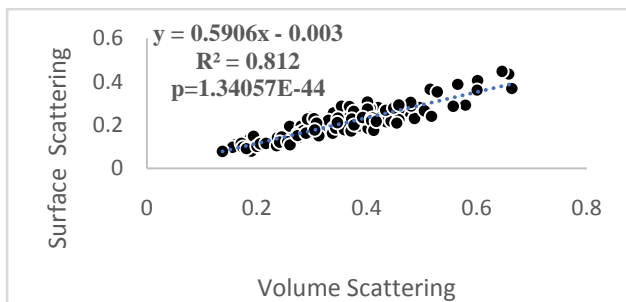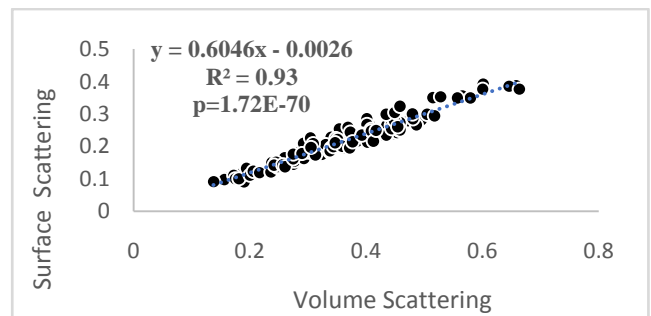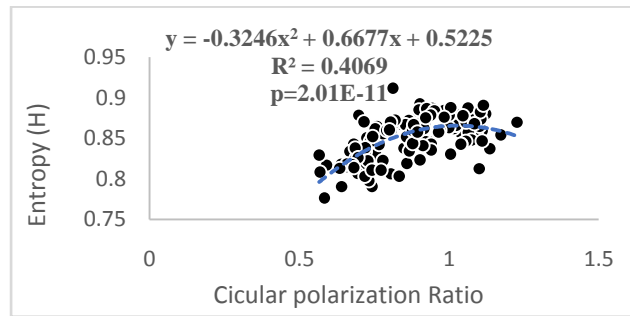
(c)

Figure 7: Plots between (a) volume scattering component of m-χ decomposition and surface scattering of m-δ decomposition, (b) volume scattering component of m-χ decomposition and surface scattering through m-χ, and (c) circular polarization ratio and the entropy (H). Note: 95% confidence bound is considered for the calculation of "p"

5. CONCLUSIONS

This study focuses on determination of the LCP index using the M^3 data and understanding the scattering mechanism of the identified LCP zones in the Bullialdus crater of the moon. The LCP index ranges between 0.01 and 0.13; majority of the data values lie within 0.01-0.08. It is observed that the LCP zones mainly occur over the central peak of the Bullialdus crater. Modified Gaussian Model fit on the spectra collected from the central peak of Bullialdus crater shows that 1 µm band is centred between 910-950nm and 2 µm band is centred between 1830-1890 nm, with relatively high Mg. Regression analysis indicates weak but statistically significant negative relation between LCP index and surface scattering, double bounce scattering, volume scattering and circular polarisation ratio (CPR); whereas, no relation is observed between LCP index and entropy (H) and mean α. More such studies are needed to better understand the scattering characteristics of different minerals on the lunar surface.

REFERENCES

Adams, J.B., 1974. Visible and near-infrared diffuse reflectance spectra of pyroxenes as applied to remote sensing of solid objects in the solar system. Journal of Geophysical Research, 79(32), pp. 4829–4836.

Barnes, A., 2016. An object-oriented classification of impact craters using Lunar Reconnaissance Orbiter data. San Francisco State University, San Francisco, California, United States.

Carter, L.M. et al., 2017. A Comparison of Radar Polarimetry Data of the Moon From the LRO Mini-RF Instrument and Earth-Based Systems. IEEE Transactions on Geoscience and Remote Sensing, 55(4), pp. 1915–1927.

Clénet, H. et al., 2011. A new systematic approach using the Modified Gaussian Model: Insight for the characterization of chemical composition of olivines, pyroxenes and olivine-pyroxene mixtures. Icarus, 213(1), pp. 404–422.

Day, J.M.D. and Moynier, F., 2014. Evaporative fractionation of volatile stable isotopes and their bearing on the origin of the Moon. Philosophical transactions. Series A, Mathematical, physical, and engineering sciences, 372(2024), pp. 1-26.

Dhingra, D., Head, J.W. and Pieters, C.M., 2017. Geological mapping of impact melt deposits at lunar complex craters Jackson and Tycho: Morphologic and topographic diversity and relation to the cratering process. Icarus, 283(Supplement C), pp. 268–281.

Gault, D.E., 1970. Saturation and Equilibrium Conditions for Impact Cratering on the Lunar Surface: Criteria and Implications. Radio Science, 5(2), pp. 273–291.

Green, R.O. et al., 2008. Moon Mineralogy Mapper Imaging Spectrometer Science Measurements. 2008 IEEE Aerospace Conference, pp. 1–5.

Horgan, B.H.N. et al., 2014. Near-infrared spectra of ferrous mineral mixtures and methods for their identification in planetary surface spectra. Icarus, 234(Supplement C), pp. 132–154.

Jin, S., Arivazhagan, S. and Araki, H., 2013. New results and questions of lunar exploration from SELENE, Chang'E-1, Chandrayaan-1 and LRO/LCROSS. Advances in Space Research, 52(2), pp. 285–305.

Klima, R.L. et al., 2011. New insights into lunar petrology: Distribution and composition of prominent low-Ca pyroxene exposures as observed by the Moon Mineralogy Mapper (M3). Journal of Geophysical Research: Planets, 116(E6), pp. 1-13.

Krishna, N. and Kumar, P.S., 2016. Impact spallation processes on the Moon: A case study from the size and shape analysis of ejecta boulders and secondary craters of Censorinus crater. Icarus, 264(Supplement C), pp. 274–299.

Kumar, S. et al., 2016. PolSAR calibration and reconstruction of hybrid polarimetric RISAT-1 data for pseudo quad-pol decomposition: a comparison with quad-pol. Proc. SPIE, 9881, p.98812C–98812C–13.

Li, Y. et al., 2017. Shape of boulders ejected from small lunar impact craters. Planetary and Space Science, 145(Supplement C), pp. 71–77.

McLeod, C.L. and Krekeler, M.P.S., 2017. Sources of Extraterrestrial Rare Earth Elements: To the Moon and Beyond. Resources, 6(3), pp. 1–28.

Melosh, H.J., 1989. Impact cratering: A geologic process, New York, USA: New York Oxford University Press.
Moynier, F. et al., 2010. Sr stable isotope composition of Earth, the Moon, Mars, Vesta and meteorites. Earth and Planetary Science Letters, 300(3–4), pp. 359–366.

NASA Reflectance Experiment Laboratory. 2016. "Modified Gaussian Model (MGM)." Reflectance Experiment Laboratory: 1–11. Retrieved June 20, 2017, from http://www.planetary.brown.edu/mgm/.

Nozette, S. et al., 2010. The Lunar Reconnaissance Orbiter Miniature Radio Frequency (Mini-RF) Technology Demonstration. Space Science Reviews, 150(1), pp. 285–302.

Osinski, G.R., Tornabene, L.L. and Grieve, R.A.F., 2011. Impact ejecta emplacement on terrestrial planets. Earth and Planetary Science Letters, 310(3), pp. 167–181.

Paniello, R.C., Day, J.M.D. and Moynier, F., 2012. Zinc isotopic evidence for the origin of the Moon. Nature, 490(7420), pp. 376–379.

Pieters, C.M. et al., 2009. The Moon Mineralogy Mapper (M³) on Chandrayaan-1. Current Science, 96(4), pp.500–505.

Pieters, C.M. et al., 2009. The Moon mineralogy mapper (M3) on Chandrayaan-1. Current Science, 96(4), pp. 500–505.

Raney, R.K., 2016. Comparing Compact and Quadrature Polarimetric SAR Performance. IEEE Geoscience and Remote Sensing Letters, 13(6), pp. 861–864.

Raney, R.K. et al., 2011. The Lunar Mini-RF Radars: Hybrid Polarimetric Architecture and Initial Results. Proceedings of the IEEE, 99(5), pp. 808–823.

Research Team, K.L. and Kramer, G., 2014. Stratified ejecta boulders as indicators of layered plutons on the Moon. Icarus, 228(Supplement C), pp. 141–148.

Robinson, M.S. et al., 2010. Lunar Reconnaissance Orbiter Camera (LROC) Instrument Overview. Space Science

Reviews, 150(1), pp. 81–124.

Smith, D.E. et al., 2017. Summary of the results from the lunar orbiter laser altimeter after seven years in lunar orbit. Icarus, 283(Supplement C), pp. 70–91.

Spudis, P.D. et al., 2013. Evidence for water ice on the Moon: Results for anomalous polar craters from the LRO Mini-RF imaging radar. Journal of Geophysical Research: Planets, 118(10), pp. 2016–2029.

Starr, R.D. et al., 2017. Crater age and hydrogen content in lunar regolith from LEND neutron data. Planetary and Space Science. (Accepted for Publication).

Sunshine, J.J.M. and Pieters, C.M.C., 1993. Estimating modal abundances from the spectra of natural and laboratory pyroxene mixtures using the Modified Gaussian Model. Journal of Geophysical Research, 98(E5), pp. 9075–9087.

Sunshine, J.M. et al., 1999. Absorption band modeling in reflectance spectra; availability of the modified Gaussian model. Lunar and planetary science, XXX; Papers presented to the Thirtieth lunar and planetary science conference., 30, p.; abstr. no. 1306.

Tomar, K.S. et al., 2016. Semi-empirical modelling for forest above ground biomass estimation using hybrid and fully PolSAR data. Proc. SPIE, 9877, pp. 987711–987729.

Vondrak, R. et al., 2010. Lunar Reconnaissance Orbiter (LRO): Observations for Lunar Exploration and Science. Space Science Reviews, 150(1), pp.7–22.

Wagner, J.K., Hapke, B.W. and Wells, E.N., 1987. Atlas of reflectance spectra of terrestrial, lunar, and meteoritic powders and frosts from 92 to 1800 nm. Icarus, 69(1), pp. 14–28.

Wang, A., Jolliff, B.L. and Haskin, L.A., 1995. Raman spectroscopy as a method for mineral identification on lunar robotic exploration missions. Journal of Geophysical Research: Planets, 100(E10), pp. 21189–21199.

Wang, K. et al., 2017. Lunar regolith can allow the synthesis of cement materials with near-zero water consumption. Gondwana Research, 44(Supplement C), pp. 1–6.

Wang, K. and Jacobsen, S.B., 2016. Potassium isotopic evidence for a high-energy giant impact origin of the Moon. Nature, 538(7626), pp. 487–490.

Wiechert, U., 2001. Oxygen Isotopes and the Moon-Forming Giant Impact. Science, 294(5541), pp. 345–348.